M. Belan, F. Messanelli
Wind Tunnel Testing of Multi-Tip Corona Actuators on a Symmetric Airfoil
Journal of Electrostatics, Vol. 85, 2017, p. 23-34
doi:10.1016/j.elstat.2016.12.002

Wind tunnel testing of multi-tip corona actuators on a symmetric airfoil

Marco Belan[a,*], Federico Messanelli[a]

[a] *Politecnico di Milano, Dipartimento di Scienze e Tecnologie Aerospaziali, via La Masa 34, 20156 Milano, Italia*

Abstract

A set of 15 different corona actuators with triangular tips on their anodes is studied by installing them on the leading edge of a NACA 0015 airfoil. Each actuator is identified by its tip sharpness and tips number/unit length. The aerodynamic forces on the airfoil are measured in the wind tunnel over a wide range of angles of attack, for different airstream velocities. The performance of the actuators is evaluated by means of several parameters, including critical and mean lift increase, drag reduction and power saving effectiveness. The best configurations are identified in terms of the above parameters.

Keywords: Plasma actuator geometry, Corona actuator, Flow control

---

1. Introduction

Corona discharge actuators are useful devices for flow control applications [1]. When a sufficiently high DC voltage is applied between two electrodes mounted on a dielectric surface, the air between the electrodes weakly ionizes. The accelerated ions, by means of collisions, transfer momentum to neutral air molecules, giving rise to an electric or ionic wind of some meters per second, that may be exploited for energizing the boundary layer. This electric wind is defined as “the movement of gas induced by the repulsion of ions from the neighbourhood of a high voltage discharge electrode” in the fundamental work of Robinson [2]. This particular kind of plasma discharge is defined as a *cold* plasma, since the energy is mainly spent to accelerate the ions, rather than to increase their temperature.

Historically, the first attempts to control a flow with an electrical discharge were performed with corona actuators during the last two decades of the last century, even though the use of a wire-to-wire corona actuator to control boundary layer transition was already reported in a paper in 1968 [3]. In more recent years, corona actuators have been

---

[*] Corresponding Author

Email address: `marco.belan@polimi.it` (Marco Belan)

Preprint submitted to Journal of Electrostatics *July 17, 2019*

studied both from a numerical [4, 5, 6, 7] and an experimental point of view [8, 9, 10, 11]. In particular, the ability of these devices in reattaching a separated flow on a flat plate has been investigated [12, 13], up to freestream velocities of 25 m/s [11]. Other applications of DC coronas include separation control on bluff bodies such as cylinders [14], modification of mixing layer properties [15], separation control of a free turbulent jet exiting from a nozzle [16] and stall control over aerodynamic airfoils [17, 18]. Different discharge regimes have been identified for increasing current values in a surface corona: following Moreau classification [1], they are called *spot*, *streamer*, *glow*, *filamentary* and *arc* regimes. In what follows we will refer to this classification, but we notice that it is not universally adopted, and other authors introduce a different terminology to indicate these phenomena, even in different geometries, as for example [19, 20]. With the surface corona configuration investigated in the present paper, the streamer and glow regimes are the most interesting for flow control, while electric arcs should be avoided, since they may excessively heat the electrodes and the dielectric surface, leading to local melting and permanent damaging of the actuator. As reported in literature, properly designed *localized arc filament plasma actuators* (LAFPA) may exploit the electric arc for high speed flow control problems [21, 22], however their geometry and operating principle are very different from the surface corona considered in this work.

In a typical surface corona, the different discharge regimes, and consequently the magnitude of the induced ionic wind, are influenced by electrical and geometrical parameters [10], mainly the applied voltage and the size and shape of the electrodes. Also the polarity of the high voltage has an effect on the actuator performance: in particular a positive corona seems more performing than a negative one, both in terms of induced velocity and electromechanical efficiency [23, 24]. Furthermore, corona discharge is very sensitive to external factors, such as the cleanliness of the dielectric surface and the relative humidity of the air [9]: a high level of humidity or a non-optimal dielectric cleaning, for instance, may greatly affect the production of ionic wind and eventually worsen the stability of the discharge, with transitions to the arc regime. For this reason, in the last years the interest of most of the scientific community shifted towards Dielectric Barrier Discharge (DBD) plasma actuators, more stable thanks to the presence of a dielectric between the electrodes [25, 26]. Thus, the literature on corona actuators applications to flow control problems is quite limited today.

The present work is focused on corona actuators with multi-tip geometry [27], where the anode is characterized by periodic triangular tips, not necessarily adjacent. This geometry is an extension of the *serrated edge* configuration, already investigated for DBDs in previous literature works [28, 29, 30]. To the authors knowledge, the multi-tip coronas have never been tested on a surface for flow control purposes, whereas an application of the serrated geometry in a volumetric discharge for a multistage ionic wind generator may be found in [31]. In [27], the authors measured at the bench the ionic wind induced on a flat plate by 12 different multi-tip coronas and compared their performances with the traditional *wire-to-plate* actuator, whose anode is made by a thin wire. The new geometry induced higher velocities and mass flows with an electro-mechanical efficiency larger than for the traditional configuration. Furthermore, the ease of ignition and the stability of the discharge are remarkably improved with the multi-tip geometry, in particular for tips of high sharpness [32]. Moreover, a comparison with traditional and multi-tip DBDs showed that multi-tip coronas are able to induce velocities similar to DBDs, although with a maximum located at a larger distance from the wall, but with a much lower power consumption, implying a higher electro-mechanical efficiency.

In the present work, a traditional wire-to-plate corona and the same 12 multi-tip geometries previously tested at the bench, with the addition of two more shapes, have been positioned at the leading edge of a NACA 0015 airfoil and tested in the wind tunnel. The effectiveness of the different shapes is evaluated in terms of lift increment and drag reduction at high angles of attack, with respect to the non-actuated case. Voltage and current measurements are also performed, in order to calculate the consumed power and the mechanical power saving due to the actuators. We wish to remark that the objective of this work is the comparison of electrodes with different shapes and not the research of the best ever performance, so that other parameters as for instance the electric field have not been set to extreme values.

2. Experimental setup

2.1. Wind tunnel and airfoil

In this experiment, a symmetric NACA 0015 airfoil (chord $c = 250$ mm, span $b = 470$ mm) is located in an open-return wind tunnel with a test section of 500×700 mm^2 in cross section and 2 m in length. The flow velocity in the test chamber can be varied from 0 to 25 m/s, with a turbulence level not larger than 0.5%.

The airfoil is made of a special kind of polyurethane, with excellent mechanical performance and insulating characteristics, and it was purposely designed for this experiment with a cavity around the leading edge. Plasma actuators are mounted on interchangeable C-shape inserts that accurately fit the cavity on the airfoil, so that the overall profile of the NACA 0015 is not modified (see §2.3). Two end plates limit the 3D effects at the lateral sides of the airfoil and help to recover an ideal two-dimensional behaviour. A rotative positioning system with optical precision (positioning accuracy $\pm 0.005°$) allows to set the angle of attack α .

In the experiment, the flow velocity is set in the range $5 \leq U \leq 20$ m/s, corresponding to Reynolds numbers based on the chord length in the interval $0.83 \times 10^5 \leq Re \leq 3.33 \times 10^5$. A particular attention has been given to $U = 10$ and 15 m/s, corresponding to Reynolds of 1.66×10^5 and 2.50×10^5 respectively. The wind tunnel is located in a large room where the temperature is controlled and kept in the range 22 ± 2 °C. The relative humidity has been maintained in the range 25 to 40 % for the entire experimental campaign. In order to account for the effects of the flow confinement between the airfoil and the tunnel walls, both solid and wake blockage corrections have been applied, following

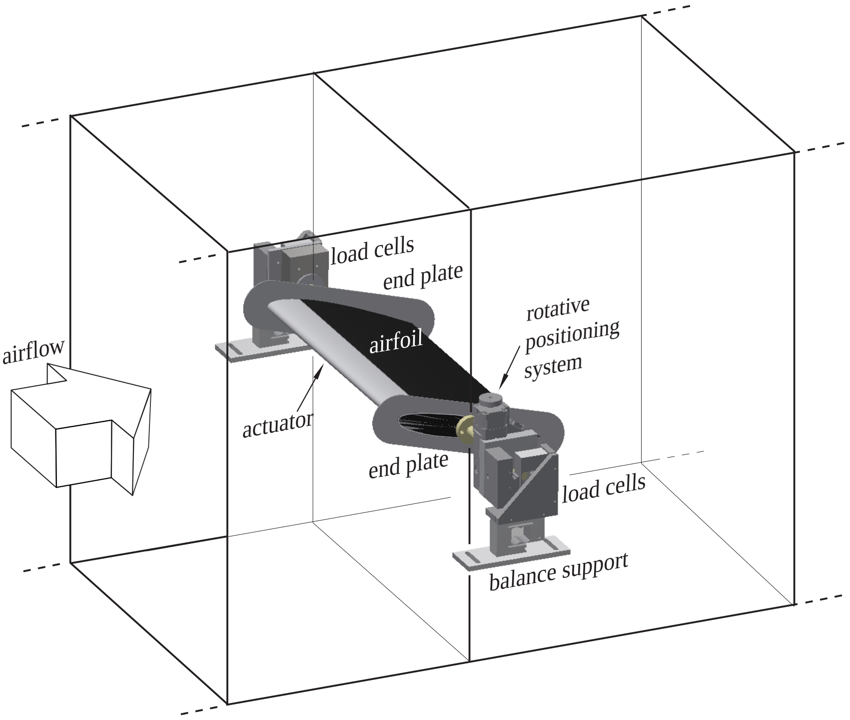

Figure 1: Experimental setup: airfoil, external balance and outline of the test section in the wind tunnel.

the procedure described in [33, 34]. All the results, and in particular the force coefficients c_l and c_d, are directly presented in corrected form.

2.2. Balance and measuring system

Lift and drag of the airfoil are measured by means of an external aerodynamic balance, purposely built for this research project. The balance has been realized from 4 load cells, symmetrically located on the two lateral sides of the test chamber. Two cells are sensitive to horizontal forces (drag) and the other two measure vertical loads (lift). The airfoil is connected to the balance by means of two lateral insulating stings. Because the output signals from the cells are in the order of millivolts, an appropriate conditioning and amplification system has been implemented to increase rejection to electro-magnetic disturbances, that can constitute an important issue in the presence of a corona discharge. The accuracy on the measured forces is ±0.2 N in the horizontal direction and ±0.4 N in the vertical one. A representation of the balance, the airfoil and the test section is presented in Fig. 1. The flow velocity in the test chamber is measured by means of the pressure jump in the contraction section located upstream: the pressure jump is acquired through suitable wall taps connected to a differential transducer, and is correlated with the velocity in the test section thanks to a previous calibration procedure carried out by means of a precision pitot probe.

The output analog signals are acquired by means of an A/D converter and digitally stored in a personal computer. Each force value is obtained as an average on a time window at least 7 s long, with a sampling rate of 4 kHz. It has been verified that this time interval is enough to reach a stationary average value, also in the post-critical range of angles of attack. The loads curves are acquired for increasing values of α in the interval 0 to 20°; the angle of attack can be increased up to 26° when needed. Before every measurement, the airfoil is always taken at zero angle of attack and then rotated to the desired value of α, in order to avoid hysteresis effects. The overall uncertainty on the force coefficients, expressed as a standard deviation, combines the uncertainties on the forces and on the flow velocities, thus it depends on the freestream velocity and moderately on the angle of attack. The values at the critical (stall) angle are well representative: for lift and drag coefficients respectively, they are $\sigma_{cl} = 0.0069$, $\sigma_{cd} = 0.0037$ at $U = 10$ m/s and $\sigma_{cl} = 0.0057$, $\sigma_{cd} = 0.0026$ at $U = 15$ m/s.

2.3. Plasma actuators and power supply

The plasma actuators are assembled on C-shape polymethyl methacrylate (PMMA) inserts that accurately fit the appositely designed cavity at the leading edge of the airfoil, as depicted in Fig. 1. The inserts are obtained from 2 mm thick PMMA sheets, thermoformed on a suitable mold so that the overall NACA 0015 shape is not modified. The junction between the airfoil and the insert has been made as smooth as possible, also with the aid of plasticine. The choice of PMMA as dielectric underlying material is supported by the work of Labergue et al. [10], where the authors measured on PMMA surfaces an increased discharge stability and ionic wind velocities higher than on every other examined material.

In the present experiment, 15 actuators are tested, each one with a different anode shape as in Fig. 2. In particular, (a) is the traditional wire-to-plate corona used as a reference and labeled C1, (b) represents 13 different multi-tip serrated edge coronas with tips of different shapes, C2 to C12, C14 and C15, and (c) is a multi-tip corona with non-adjacent tips (C13). In Fig. 2 they are represented in flat form for clarity, but when mounted on the airfoil they assume the local curvature of the leading edge, as shown in Fig. 3. The names of the actuators follow the convention introduced in the previous tests at the bench [27]: in particular, the 13 actuators labeled C1 to C13 have been successfully tested, whereas C14 and C15 could not be correctly ignited in initially still air, because of their tendency to arcing. However, they have been added in this work because their wind tunnel tests are possible, thanks to the increased stability of the discharge in the presence of an external flow, as known in literature [15].

All the electrodes are made of aluminium tape, 0.12 mm thick, with the exception of the anode of actuator C1, which is a copper wire, 0.1 mm in diameter. The electrodes gap is always $g = 15$ mm. The anode tips and the wire of C1 are always aligned with the leading edge (Fig. 3), so that the plasma discharge always starts exactly at the leading edge, since it is known that the flow control authority is maximized when the actuation is

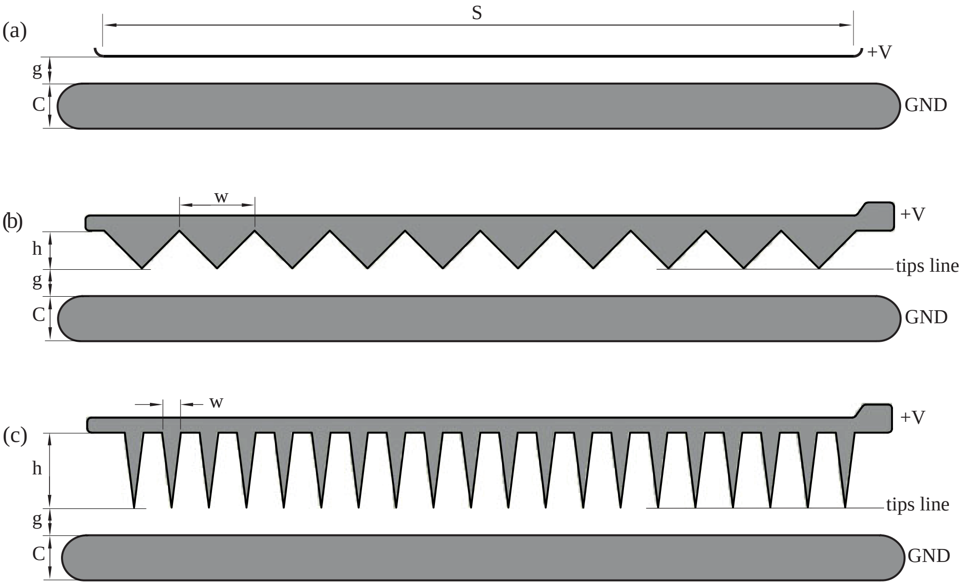

Figure 2: Geometries of the 15 coronas in flat form: (a) straight wire-to-plate (C1); (b) multi-tip, serrated (C1...C12, C14, C15); (c) multi-tip, separated tips (C13).

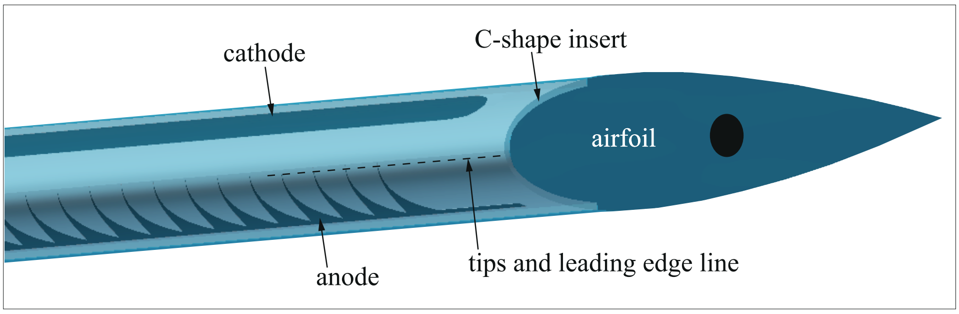

Figure 3: Details of an actuator assembled on the leading edge.

located upstream or near the separation point [18, 35]. All the actuators have a working span of $S = 400$ mm, which means that they cover approximately the 85% of the airfoil span. The chordwise length of the cathode is always $C = 25$ mm.

The different anodes are parameterized by means of their tips height h, width w and number N, as indicated in Tab. 1. Starting from these geometrical quantities, it is possible to define two new parameters, i.e. the tips density (tips number per unit length) $n = N/S$ and the tip sharpness $r = h/w$, that identify a parameter space useful to present the results:

$$(n, r) = \left(\frac{N}{S}, \frac{h}{w}\right). \tag{1}$$

This choice resulted particularly meaningful in the previous experiment at the bench [27],

Table 1: Geometrical parameters of the corona actuators under test.

Name	h [mm]	w [mm]	$n = N/S$ [m^{-1}]	$r = h/w$
C1	0	–	–	0
C2	8	4	250	2
C3	8	5	200	1.6
C4	10	10	100	1
C5	15	10	100	1.5
C6	20	4	250	5
C7	20	5	200	4
C8	20	8	125	2.5
C9	20	10	100	2
C10	20	20	50	1
C11	30	10	100	3
C12	40	10	100	4
C13	40	10	50	4
C14	3	10	100	0.3
C15	5	10	100	0.5

since the induced ionic wind is strongly sensitive to both the above defined parameters, and also in this work the compared results will be presented in the (n, r) space.

The actuators are operated by a high voltage DC power supply unit capable of ±20 kV and 6 mA. The anodes are connected to the positive pole through a low-pass T filter ($R_a = 4.4$ MΩ, $C = 0.9$ nF, $R_b = 4.4$ MΩ). The resistance R_b works as ballast and the filter avoids undesired power breakdowns, since the PSU is equipped with a safety circuit that turns the power off when detects a spark. The cathodes are grounded through a non inductive shunt resistor ($R_s = 100$ Ω), useful for current measurements, whereas the voltage between the electrodes is measured by means of a 1:1000 voltage divider (load 47 MΩ). All the actuators are supplied with a positive voltage $V_0 = 16$ kV upstream of the filter, with the exception of the wire-to-plate, which requires a slightly higher voltage of $V_0 = 17$ kV to correctly ignite in the streamer regime as the other devices. Voltage and current signals are acquired by means of a digital oscilloscope at a sampling frequency of at least 100 MHz. It should be noticed that the averaged current value directly read on the PSU instrument is in excellent agreement with the acquired signal. It has been verified, by means of the current value displayed on the PSU internal monitor, that the presence of the shunt resistor does not significantly affect the measurements. Further details on the electrical setup may be found in [27]. The electric power is calculated by averaging the product $P = VI$ and the combined uncertainty is ±1 W with a 95 % confidence level.

3. Results

The set of actuators has been tested by acquiring the force coefficients at different velocities. The main body of results has been obtained working at freestream velocities U=10 and 15 m/s for $0 \leq \alpha \leq 20°$; when necessary for completeness, some additional tests have been performed on the extended ranges $5 \leq U \leq 20$ m/s and $0 \leq \alpha \leq 26°$. This section presents at first a selection of detailed sample cases, then a complete comparison of the actuators performances, made in the parameter space defined by Eq. (1).

3.1. Data of sample actuators

In this work, the performance of the actuators is evaluated on the field, by means of measurements of force coefficients on an airfoil. Before analyzing the dependence of the active flow control on the tips geometry, we checked the effects of the actuators as passive (unpowered) devices with respect to a smooth profile, because of their small interaction with the boundary layer, due to the finite thickness of the electrodes and to their shape. Afterwards, all the results are presented in relative terms, i.e. measuring the changes of the force coefficients when a given actuator already installed on the airfoil is turned on.

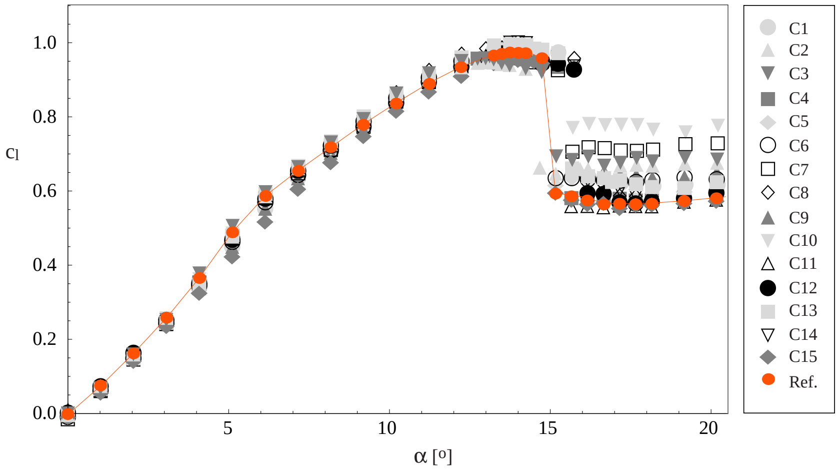

Figure 4: $c_l(\alpha)$ at U =15 m/s for the actuators turned off, compared with the reference without electrodes (reference points linearly connected for readability).

The behaviour of the airfoil equipped with the different actuators turned off is presented in Fig. 4 at U =15 m/s, or $Re = 2.5 \times 10^5$. The figure includes as a reference the data for the 0015 airfoil with the PMMA leading edge section devoid of electrodes. The $c_l(\alpha)$ curves are similar to the reference one up to the critical range, where many devices shift the c_l drop to larger angles. In the following post-critical range, the trend of $c_l(\alpha)$ returns similar to the reference one, but biased toward higher values. In particular, the actuators C2,C3,C7 and C10 give in this range a c_l more than 10% higher than the reference.

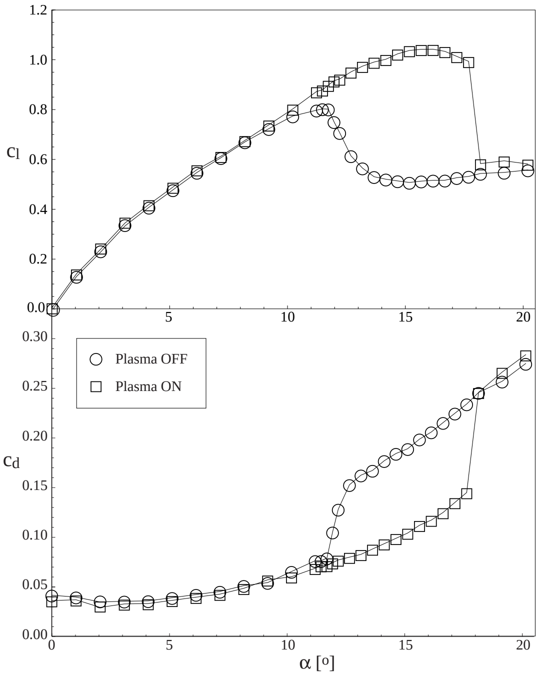

Figure 5: Actuator C6 at U=5 m/s: $c_l(\alpha)$ and $c_d(\alpha)$ with plasma off and on. Data linearly connected.

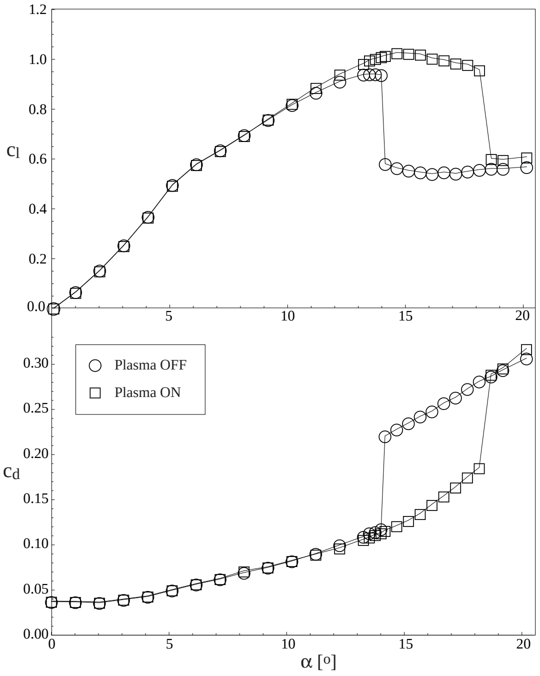

Figure 6: Actuator C6 at U=10 m/s: $c_l(\alpha)$ and $c_d(\alpha)$, plasma off and on. Data linearly connected.

A computation made by the software XFoil [36] shows that about the critical angle α_c of maximum lift, for U =10 and 15 m/s the 0.12 mm thickness of the electrodes is small but not negligible with respect to the boundary layer thickness. Here the unpowered electrodes play the role of manipulators in a boundary layer that would anyway become turbulent in the same zone: actually, under these conditions the transition over a smooth 0015 airfoil would occur spontaneously at a distance in the order of 20 mm downstream of the leading edge and the electrodes could only slightly move the transition location. Indeed the dispersion of the $c_l(\alpha)$ curves in the post-critical range at U=10 and 15 m/s is similar. Actually, also at the lower velocity U=5 m/s the curves dispersion is similar, but the involved mechanism is different, since in this case the original boundary layer in the actuators zone is laminar, and all the electrodes act as turbulators, probably causing the transition.

About the reference data, it is worth noting that their validity is limited to the present experiment: in fact, the corresponding curves in literature are quite dispersed, mainly because of the tridimensionality of the real flow around a wind tunnel airfoil. At similar Reynolds numbers, different experiments on the same airfoil give remarkable variations of c_l in the critical and post-critical range [37, 38, 39], depending on the span/chord aspect ratio of the model and on the size of the end plates.

When the actuators are switched on, they modify the force coefficients, improving the aerodynamic performance. This effect is large at low airstream velocities (U = 5 m/s in

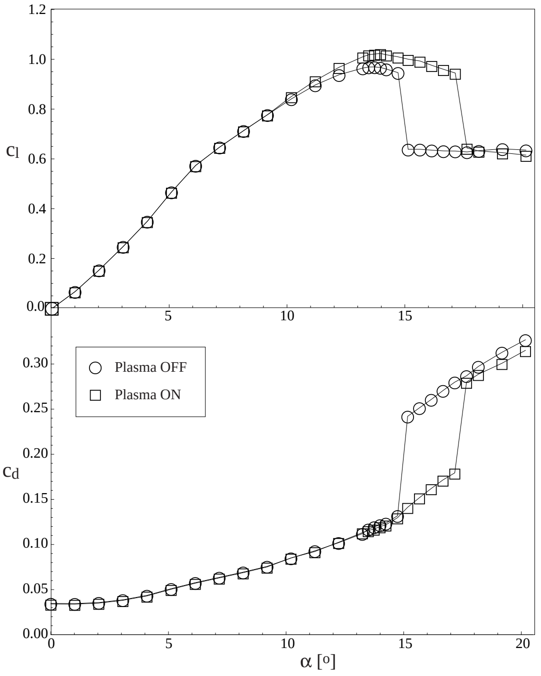

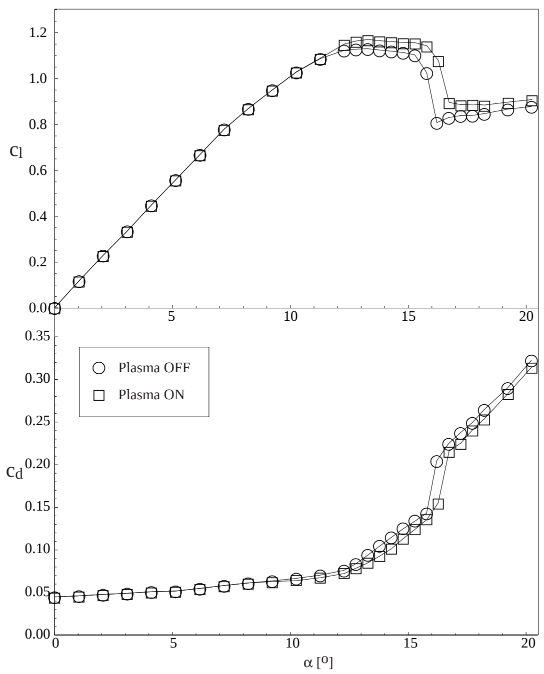

Figure 7: Actuator C6 at U=15 m/s: $c_l(\alpha)$ and $c_d(\alpha)$, plasma off and on. Data linearly connected.

Figure 8: Actuator C6 at U=20 m/s: $c_l(\alpha)$ and $c_d(\alpha)$, plasma off and on. Data linearly connected.

this experiment), whilst it decreases as U grows. Figs. 5 to 8 show a significant example, reporting the variations of $c_l(\alpha)$ and $c_d(\alpha)$ given by the same actuator (C6) for increasing values of U. Qualitatively, all the multi-tip actuators under test behave as in these figures, of course with different effectiveness. In Fig. 5, the performance at the lowest point of the present velocity range is outstanding, but this is just a confirmation of the other literature studies carried out at low airstream velocities, comparable with the ionic wind given by the actuator. In the following figures, 6 to 8, the velocity U is progressively increased whilst the performance worsen, but even at the highest velocity $U = 20$ m/s the actuator is still effective in terms of lift increase and drag reduction. In general, the changes of the lift coefficient c_l are negligible for small angles of attack, whereas the top value $c_{l,max}$ is increased by the actuators, the corresponding critical angle α_c is also increased and the whole stall range is shifted toward larger angles. Also the variations of the drag coefficient c_d are generally small or negligible for a wide range of angles, up to values slightly larger than α_c; instead, the actuator effect is clearly visible in the stall range. Here the lift drop and drag rise, that occur at the same angle when plasma is off, are shifted together toward a larger angle when plasma is turned on.

3.2. Comparisons in the parameter space

In order to carry out a compared analysis of the whole set of actuators, it is necessary to introduce suitable parameters to quantify the performance of the corona devices under test, as explained in what follows and visualized in Fig. 9. An important parameter is

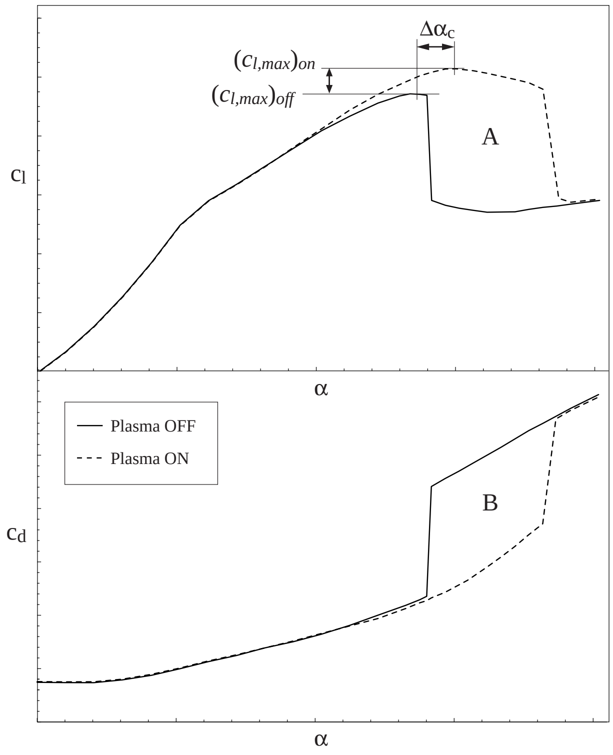

Figure 9: Sketch for the definitions of performance parameters.

the increase of the maximum lift, or lift increase at critical point, obtained by turning the plasma on. In Fig. 9, it is the vertical distance between the values of $c_{l,max}$ with and without the plasma discharge. Referring this quantity to the plasma off value, it takes the form

$$\Delta c_{l,max} = \frac{(c_{l,max})_{on} - (c_{l,max})_{off}}{(c_{l,max})_{off}} \tag{2}$$

and can be reported in percentage form. As seen in the previous subsection and in Fig. 9, the maximum lift coefficients $(c_{l,max})_{off}$ and $(c_{l,max})_{on}$ are generally measured at different critical angles α_c: since α_c grows when plasma is turned on, also this shift could be used as a parameter:

$$\Delta\alpha_c = (\alpha_c)_{on} - (\alpha_c)_{off}. \tag{3}$$

Besides the local quantities $\Delta c_{l,max}$ and $\Delta\alpha_c$, also the global variations of the whole $c_l(\alpha), c_d(\alpha)$ curves can be considered as significant parameters. In normalized form they can be defined over a suitable domain $0 \leq \alpha \leq \alpha_M$ as

$$\langle \Delta c_l \rangle \;=\; \frac{\int_0^{\alpha_M} [(c_l)_{on} - (c_l)_{off}]\, \mathrm{d}\alpha}{\int_0^{\alpha_M} (c_l)_{off}\, \mathrm{d}\alpha}, \tag{4}$$

$$\langle \Delta c_d \rangle \quad = \quad \frac{\int_0^{\alpha_M} [(c_d)_{off} - (c_d)_{on}]\, \mathrm{d}\alpha}{\int_0^{\alpha_M} (c_d)_{off}\, \mathrm{d}\alpha} \tag{5}$$

and in Fig. 9 the numerators of these formulas are the areas labeled as A and B. From Figs. 5...8 it is clear that the main contributions to the integrals in the numerators above are due to the large areas between the on and off curves in the post-critical range. The integrals become independent of α_M if this angle is chosen sufficiently high, in the range where the on and off curves return to coincide within the accuracy level. The value $\alpha_M = 20^\circ$ used in the $c_l(\alpha)$ plots of §3.1 does not satisfy this requirement for all tests, so that in some cases additional data at larger angles have been acquired. Setting $\alpha_M = 26^\circ$ has led to $\langle \Delta c_l \rangle$ and $\langle \Delta c_d \rangle$ values independent of α_M for all the actuators at U=10 m/s, whereas at 15 m/s 4 devices out of 15 would still require higher α_M, leading to measurement conditions with excessive flow confinement. Thus, global data for $\langle \Delta c_l \rangle$ and $\langle \Delta c_d \rangle$ are presented only at U=10 m/s.

Before comparing the different actuators on the basis of the parameters defined above, another operation must be done on the original data: in fact, the unavoidable errors that act on each single datum may negatively affect the parameters relying on the off-to-on differences, and this is particularly true for the local quantities as $\Delta c_{l,max}$, that takes values gradually lower for increasing airstream velocities. For these reasons, the original c_l and c_d data are suitably interpolated before using them in the calculations of the parameters (2) to (5). The interpolations are obtained by means of matched polynomials calculated by the least squares method: for example, the Fig. 10 shows the $c_l(\alpha)$ curve at U=15 m/s for the actuator C9 turned off. The interpolating function $F(\alpha)$ is made of 2 matched polynomials and is superimposed to the original data with their error bars. The length of the bars in terms of standard deviations is $2\,\sigma_{cl}$, and the validity of the fit is confirmed by comparing $\sigma_{cl} = 0.0057$ with the mean square distance of the fit from the K data points, $\chi = [\Sigma_i (F_i - c_{l,i})^2/K]^{1/2} = 0.0039$: χ and σ_{cl} are in the same order of magnitude, and have similar values. For all the curves considered in this study, the polynomials are determined in such a way as to satisfy this condition.

In what follows, the c_l and c_d curves are used to calculate the parameters $\Delta c_{l,max}$, $\Delta\alpha_c$, $\langle \Delta c_l \rangle$ and $\langle \Delta c_d \rangle$ for each actuator under test. The results are presented in the parameter space (n, r) defined by Eq. (1), where each actuator lies on a given point, with the exception of the straight C1, represented by the line $r = 0$. The resulting maps like $\Delta c_{l,max}(n, r)$ are then visualized as interpolated surfaces to give an easier readability with respect to data tables. The visible surfaces should be taken mainly as a guide to evaluate the actual data values, since the data point density corresponding to the different devices is inhomogeneous. However, the minimum and maximum values are always indicated, as well as the most significant values.

The figures 11 and 12 show the $\Delta c_{l,max}$ values given by the actuators at U =10 and 15 m/s. The highest $\Delta c_{l,max}$ in Fig. 11 is 9.6%, given by the actuator C2 (250,2). The accuracy of the values in Fig. 11 is ±1%: in general, all the results presented in this section

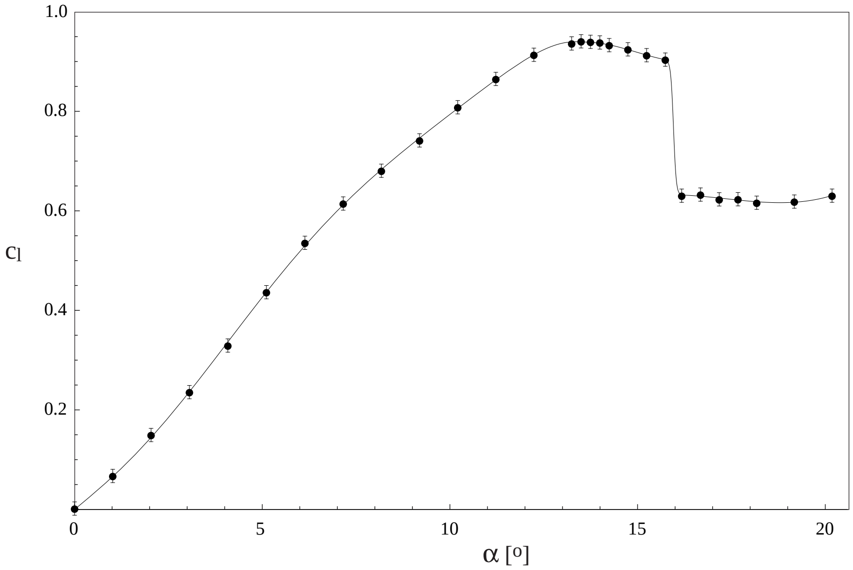

Figure 10: Interpolated $c_l(\alpha)$ for actuator C9 at U =15 m/s, plasma off.

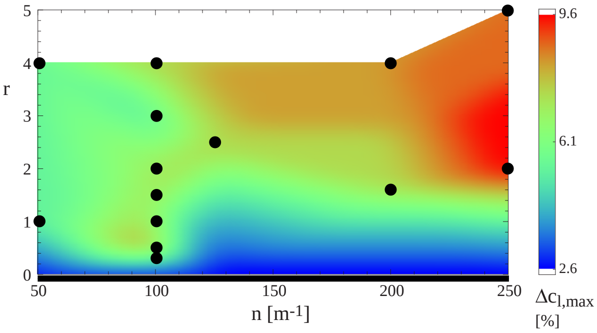

Figure 11: Map of $\Delta c_{l,max}$ at U=10 m/s.

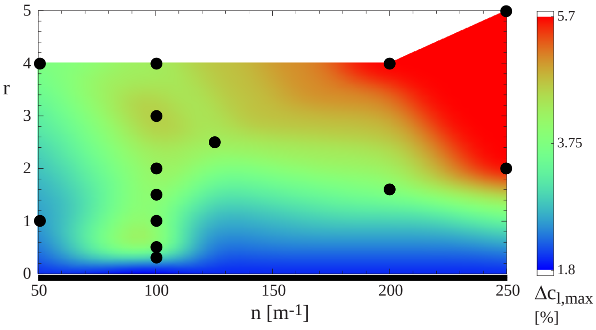

Figure 12: Map of $\Delta c_{l,max}$ at U=15 m/s.

are affected by the combined uncertainties of $(c_l)_{on}$ and $(c_l)_{off}$ or $(c_d)_{on}$ and $(c_d)_{off}$, so that their error bands are larger than for the original data. At U =15 m/s, the best actuator of Fig. 12 in terms of $\Delta c_{l,max}$ remains the C2 with 5.7%, but two other devices give very close values, namely C6 (250,5) with 5.6% and C7 (200,4) with 5.4%. The accuracy for this figure is ±0.8%. At U=20 m/s the actuators give small $\Delta c_{l,max}$, in some cases comparable with the data uncertainty, so that the map becomes difficult to produce, but the best device seems to be C6 with $\Delta c_{l,max}$=3.5%. In general, the most effective actuators in these maps are located on their upper right zones: all these devices are characterized by numerous tips ($n \geq 200$) and high sharpness ($r \geq 2$), so that they create a large number of small jets at the wall. Within the set under study, these actuators give also the highest mass flows Q at the bench, as shown by the authors in [27]. Assuming that the discharge works by adding kinetic energy to the airstream in the boundary layer region, a possible interpretation of these results can be proposed by relating the lift increase to an energy ratio:

$$\Delta c_{l,max} = k \left(\frac{u_b}{U} \right)^2 \tag{6}$$

where k is a constant and u_b is the bulk velocity corresponding to a given mass flow $Q = \rho u_b A$ through a surface A normal to the ionic wind and to the wall. Relying on the cited mass flow data [27], Fig. 13 shows for 3 sample actuators that Eq. (6) may approximately fit the trends of $\Delta c_{l,max}$ over the considered airstream velocity range. Much better fits can be easily obtained by including linear terms.

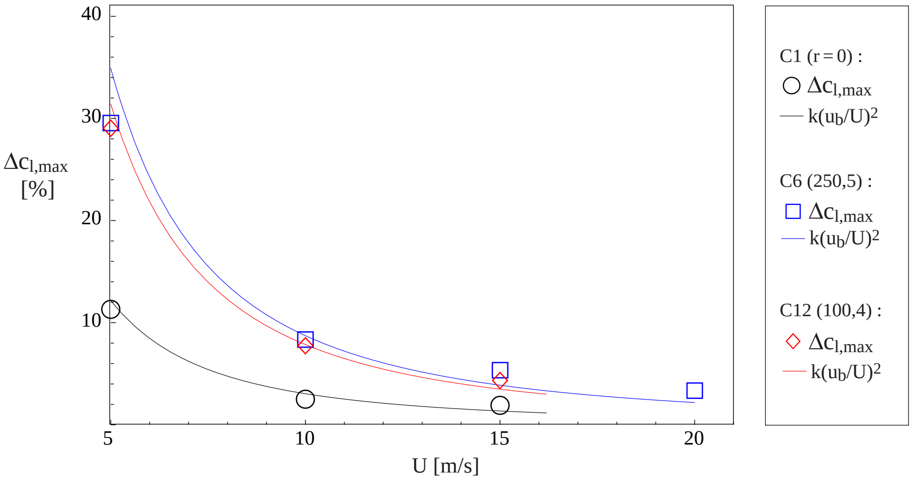

Figure 13: $\Delta c_{l,max}$ as function of airstream velocity U for 3 actuators and comparison with Eq. (6).

The critical angle shift $\Delta\alpha_c$ takes large values only in the tests at U=5 m/s, whilst for larger airstream velocities the increase of α_c can become small and less regular over the (n, r) domain; also the differences between actuators become small, so that it is difficult to present the results by means of maps. Furthermore, even if the angular position of the airfoil is known with high precision, the overall accuracy on $\Delta\alpha_c$ is in the order of $\pm 0.2°$, so that the measurements of very small $\Delta\alpha_c$ are quite unreliable. This is due to the very weak crossflow in the airstream, since in a real wind tunnel the test section streamlines are not perfectly parallel, and the residual tiny vertical velocities in the test section affect the angular measurements. In general, a good performance in terms of $\Delta\alpha_c$ does not appear related to high values of $\Delta c_{l,max}$, but there are exceptions as the actuator C7 (200,4), that exhibits similar trends for $\Delta c_{l,max}$ and $\Delta\alpha_c$ as U increases: for $U = 5, 10$ and 15 m/s it gives respectively $\Delta c_{l,max} = 29.4\%, 8.4\%, 5.4\%$ and $\Delta\alpha_c = 4.5°, 0.9°, 0.7°$.

In Figs. 14 and 15, the actuators are evaluated on the basis of the integral parameters $\langle\Delta c_l\rangle$ and $\langle\Delta c_d\rangle$, with accuracies of $\pm 1.2\%$. Considering $\langle\Delta c_l\rangle$, the best actuators are C2 (250,2) with $\langle\Delta c_l\rangle$=18.8% and C6 (250,5) with 17.9%, whereas secondary regions of

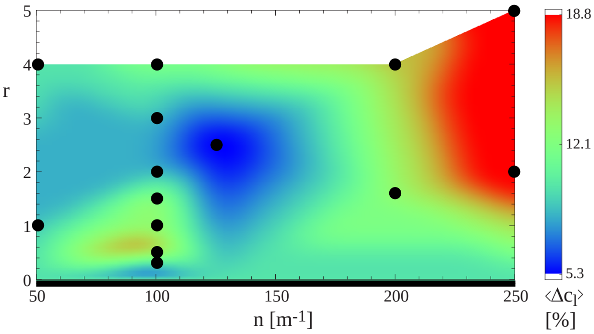

Figure 14: Map of $\langle \Delta c_l \rangle$ at U=10 m/s.

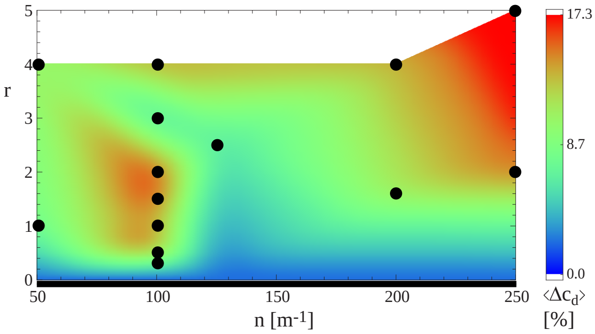

Figure 15: Map of $\langle \Delta c_d \rangle$ at U=10 m/s.

good performance are created between C15 (100,0.5) and C4(100,1), and also between C11 (100,3) and C12 (100,4). It is also important to notice that the simple wire-plate C1, that gives $\langle \Delta c_l \rangle$=13.1%, is not the worst device. Excluding the wire-plate, this map is not very different from Fig. 11, and it seems that the multi-tip devices creating a good local lift increase $\Delta c_{l,max}$ are also effective in creating a mean increase $\langle \Delta c_l \rangle$ along the angular range. In terms of $\langle \Delta c_d \rangle$, the best actuator is C6 (250,5) with $\langle \Delta c_d \rangle$=17.3%, whereas C2 (250,2) gives 15.1% and some actuators with $n = 100$ m^{-1} give good values, above 14%. Some of these actuators are well performant also in terms of $\langle \Delta c_l \rangle$, but this is not a general property: in fact, here C1 gives only $\langle \Delta c_d \rangle$=2.1%. However, the maps are similar and it is evident that a high number of sharp tips ($n \geq 200$ m^{-1}, $r \geq 2$) is beneficial both in terms of $\langle \Delta c_l \rangle$ and $\langle \Delta c_d \rangle$.

The main point to consider in understanding Fig. 14 is the effectiveness of the actuators in the stall range: the mean lift increase $\langle \Delta c_l \rangle$ takes on large values when there is a large distance between the curves $c_l(\alpha)_{on}$ and $c_l(\alpha)_{off}$, and this always happens for $\alpha > \alpha_c$, i.e. in the post-critical or stall range, as visible for example in Figs. 5 to 8. The shape of the curves in this zone is not related to the local maximum achieved at α_c, that is to the maximization of the ionic wind flow, but rather to the complex interaction of the actuator flow with the external field of motion, that without the plasma effect would be separated from the body. Further details are given in Fig. 16, that presents the same 3 devices considered in Fig. 13, but comparing their behaviours in terms of $\Delta c_{l,max}$ and $\langle \Delta c_l \rangle$ as U grows from 5 to 15 m/s: $\Delta c_{l,max}$ decreases in similar way $\sim 1/U^2$ for all the actuators, but the trends of $\langle \Delta c_l \rangle$ are different. In particular, $\langle \Delta c_l \rangle$ for the wire-plate C1 is only slightly influenced by U, whilst $\langle \Delta c_l \rangle$ for the multi-tip C6 (250,5) and C12 (100,4) decreases rapidly, until at U=15 m/s C6 becomes less performant than C1.

3.3. *Effectiveness parameters*

The effectiveness of the actuators in terms of power saving is another important field of characterization. For the definition of significant effectiveness parameters we were inspired by the work of Kriegseis et al. [40], although our parameters are considerably

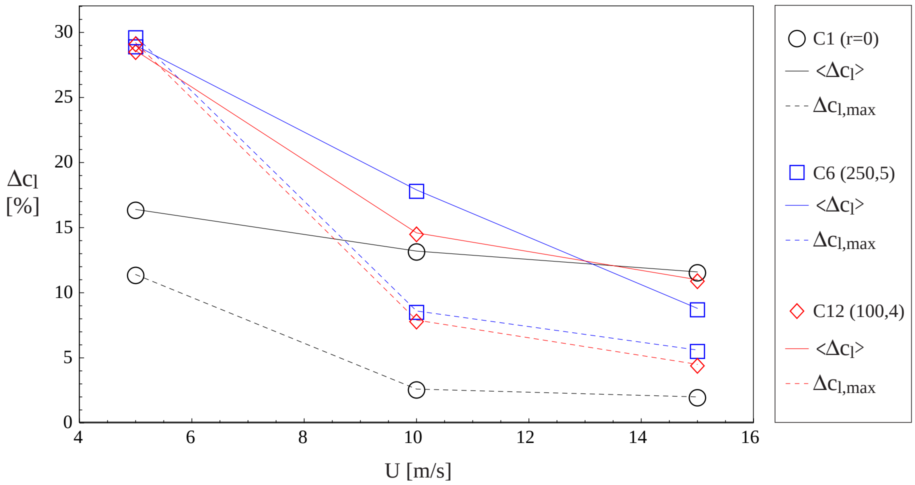

Figure 16: Comparison of $\langle \Delta c_l \rangle$ and $\Delta c_{l,max}$ as function of airstream velocity U for 3 actuators.

different, since this work is specifically focused on actuators applied to an airfoil. Here, in order to define suitable parameters, it is useful to introduce the power needed to lift a load, referring to the typical purpose of an airfoil. Lifting a load (force) L with vertical velocity U_z requires a power

$$P_z = U_z L, \tag{7}$$

and turning the corona on, the power variation for constant U_z is

$$\Delta P_z = U_z \Delta L \tag{8}$$

so that, considering the electric power W_e supplied to the actuator, a lift effectiveness parameter can be defined in nondimensional form as

$$\eta_l = U_z \Delta L / W_e \ . \tag{9}$$

This is a power saving ratio, not to be confused with a thermodynamic efficiency, and values $\eta_l > 1$ indicate that a given electric power controls a larger mechanical power. The definition (9) must be better specified by focusing on ΔL: as a first choice, this force variation can be assumed as the maximum lift increase occurring under critical conditions

$$\Delta L_{max} = \frac{1}{2} \rho U^2 bc \left[(c_{l,max})_{on} - (c_{l,max})_{off} \right] \tag{10}$$

that is obviously related to the $\Delta c_{l,max}$ defined above, through the velocity U, the density ρ and the reference surface bc (airfoil span×chord). This gives rise to the parameters

$$\eta_{lc} = U_z \Delta L_{max} / W_c \tag{11}$$

$$\varepsilon_{lc} = \eta_{lc} / U_z = \Delta L_{max} / W_c \ , \tag{12}$$

referred to the power consumption W_c under critical conditions (stall angle); the critical lift effectiveness ε_{lc} in N/W or s/m is of practical use when U_z is unknown. Furthermore, the definition (9) can also be extended by introducing the mean lift variation, in the following way:

$$\eta_{lm} \;=\; U_z \left\langle \Delta L/W_e \right\rangle \;=\; U_z \int_0^{\alpha_M} \frac{L_{on} - L_{off}}{W_e}\, \mathrm{d}\alpha. \tag{13}$$

Here the electric power W_e can not be factorized because in general it depends on the local flow velocity on the actuator and thus on the angle of attack α. As above, when U_z is unknown a corresponding parameter can be defined for the practical use:

$$\varepsilon_{lm} \;=\; \eta_{lm}/U_z = \left\langle \Delta L/W_e \right\rangle \;. \tag{14}$$

Finally, also the mean drag variation can lead to the definition of an effectiveness parameter:

$$\eta_{dm} \;=\; U \left\langle \Delta D/W_e \right\rangle \;=\; U \int_0^{\alpha_M} \frac{D_{off} - D_{on}}{W_e}\, \mathrm{d}\alpha. \tag{15}$$

In this case, η_{dm} is nondimensional and directly referred to the freestream velocity U.

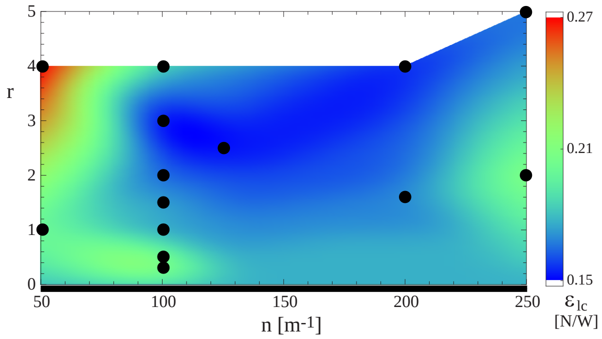

Figure 17: Map of critical lift effectiveness ε_{lc} at U=10 m/s.

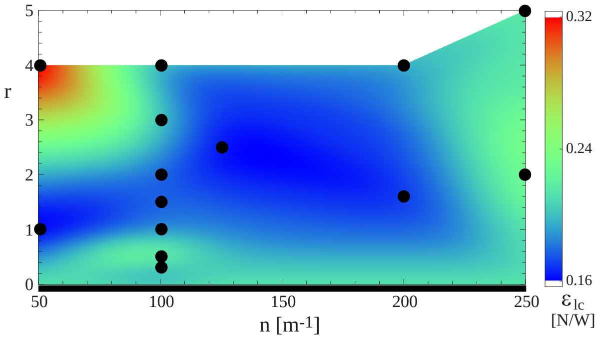

Figure 18: Map of critical lift effectiveness ε_{lc} at U=15 m/s.

The maps of critical lift effectiveness ε_{lc} at U =10 and 15 m/s are shown in Figs. 17 and 18, respectively. The highest value in Fig. 17 is 0.27 N/W and corresponds to the device C13 (50,4), with an accuracy of ±0.03 N/W; also the local maximum ε_{lc}=0.23 N/W given by C2 (250,2) is noteworthy, since this device is the best performant in terms of $\Delta c_{l,max}$. At U =15 m/s, the most effective remains C13 with ε_{lc}=0.32 N/W with accuracy ±0.03 N/W, whereas on the right border the actuators with high $\Delta c_{l,max}$ maintain good values: C2 and C6 give respectively 0.26 and 0.24 N/W. Among the others, the wire-plate C1 should also be mentioned with its value ε_{lc}=0.23 N/W. These maps are essentially determined by the balance between $\Delta c_{l,max}$ and W_c, the electric power in the denominator

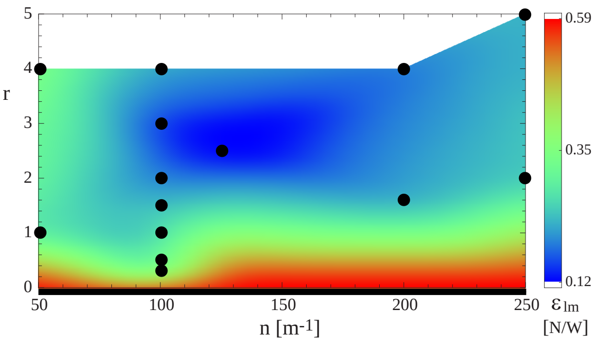

Figure 19: Map of mean lift effectiveness ε_{lm} at U=10 m/s.

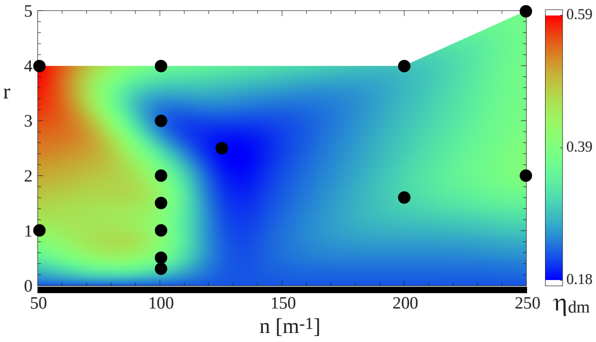

Figure 20: Map of mean drag effectiveness η_{dm} at U=10 m/s.

of Eq. (12). In turn, the power consumption is approximately related to the tips density n, so that devices having low consumptions can have good effectivenesses even if they are not so performant in increasing the lift. For example, at U=15 m/s, C1 (no tips) needs only W_c=1.3 W and the power for C13 (50,4) is 2.3 W, whilst W_c is 3.4 W for C2 (250,2) and 3.7 W for C6 (250,5).

The map of mean lift effectiveness ε_{lm} at U =10 m/s is shown in Fig. 19, with accuracy ±0.07 N/W. Here the parameter ε_{lm} is mainly determined by the power consumption of the actuators, so that the best values are given by the wire-plate C1, that needs the lowest power to work. These data depend also on the shape of the curve $W(\alpha)$ that expresses the electric power as function of α for each actuator; however, the trend of $W(\alpha)$ is similar for the whole set, and does not introduce remarkable differences. In general, the value W_c required by a given actuator at the critical angle α_c remains nearly the same in a wide range of post-critical angles. For angles $\alpha < \alpha_c$ instead, as α decreases, a slight and monotonic decrement of $W(\alpha)$ is recorded for all the actuators, that require about $0.7W_c$ for $\alpha = 0$, but in this range the effect of the discharge on the c_l and c_d curves is negligible.

The parameters ε_{lc} and ε_{lm} are in general smaller than 1 N/W, but multiplying them by a moderate vertical velocity U_z, even smaller than U, the resulting nondimensional effectivenesses η_{lc} and η_{lm} may become much larger than 1, what proves the advantage in using these actuators. Furthermore, the trend with U is promising, since the available date show that η_{lc} and η_{lm} tend to increase for higher values of the airstream velocity.

The mean drag effectiveness η_{dm} is shown in Fig. 20 with accuracy ±0.08. In this figure, the best value η_{dm}=0.59 is given by C13 (50,4), and several other actuators give good values $\eta_{dm} > 0.4$, in the regions $n = 100$ m^{-1} and on the right border ($n = 250$ m^{-1}). Also in this case, the values of η_{dm} estimated from the available data seem to increase for increasing velocities: for example, η_{dm} for C13 grows from 0.59 at $U = 10$ m/s to 0.81 at $U = 15$ m/s, and other actuators exceed 0.9.

The examination of Fig. 20 reveals that this map is roughly related to the $\langle \Delta c_d \rangle$ map of Fig. 15. The dependence of η_{dm} on (n, r) is quite complicated, but in general the best values are found for high r, i.e. the tip sharpness is important in reducing the drag. Nevertheless, even for the best actuators the values of η_{dm} are slightly smaller than 1, so that for $U \leq 15$ m/s the drag reduction alone is not large enough to create a net power saving. The threshold $\eta_{dm} = 1$ might probably be exceeded at U=20 m/s, but the uncertainty of the relevant data in the present study is not small enough to carry on reliable comparisons.

4. Discussion and Conclusions

In this experiment, a set of 15 corona actuators has been tested in the wind tunnel. The devices are multi-tip actuators, i.e. the contours of their anodes have periodic triangular tips, even not adjacent; the geometry of each actuator is set by the tips number per unit length n and the tip sharpness r (height/width ratio), that define a parameter space (n, r). The tests have been carried out on the basis of the aerodynamic performance of a symmetric airfoil, equipped with the actuators under test. As a reference, a straight wire-to-plate corona has been included among the devices under test.

The effects of the actuators on the aerodynamics of the airfoil have been studied by means of several parameters. A first parameter, important in stall delay applications, is the maximum achievable lift at the critical angle of attack α_c: all the multi-tip corona increase the maximum lift of the airfoil, overcoming the standard wire-to-plate actuator. When plasma is turned on, the whole stall range moves toward larger angles of attack, and also the critical angle α_c is generally shifted toward moderately larger values. The best devices turn out to have high n and r, i.e. numerous and sharp tips. The effect of the actuators on the maximum lift, as known in literature, decreases for increasing airstream velocities U, in a similar way for all the devices.

Also in applications where the main parameter is the mean lift increase over a wide angular range, the best devices have numerous sharp tips. However, in this case the wire-to-plate is not the worst device, and only the best multi-tip coronas overcome its performance, so that the identification of an optimal geometry is particularly important.

When the actuators are compared on the basis of the mean drag reduction over the angular range, all the multi-tip coronas perform better than the wire-plate. In this field, high values of sharpness r are important, but there are other regions of good performance in the (n, r) plane.

The set of actuators has been also considered in terms of power saving, i.e. of ratios of saved mechanical power and consumed electric power. Three different parameters have been introduced, referring the effectiveness (power saving) of the devices to the maximum lift increase, the mean lift increase, and the mean drag reduction. The effectiveness under maximum lift conditions seems only weakly related to the good performance of the actuators, instead it is mainly determined by the electric power consumption, so that the most effective coronas are the ones that need less input power, even if their lift increase is moderate. The effectiveness in increasing the mean lift along a wide angular range gives an interesting result: here the wire-to-plate is the best actuator, since it works over a wide angular range whilst it needs a remarkably low input power. Finally, the effectiveness in reducing the mean drag over the angular range is generally high for actuators with high sharpness.

The experimental technique adopted in this work does not permit to give local details about the changes induced in the flow by different actuators. However, by comparing the present results with the tests made at the bench on the same devices [27], the main mechanism involved seems to be the creation of periodic parallel jets at the wall, capable of energizing the lower part of the boundary layer. In fact, the best devices in creating a useful lift increase are mainly the ones with numerous and sharp tips (large n and r), that can create a large number of effective jets, and give also high values of mass flow in still air the bench. Instead, the existence of local minima and secondary maxima in the lift maps could depend on flow structures corresponding to spanwise modes, excited by the periodicity of the actuators. Such structures have already been observed in flows controlled by plasma actuators [41, 42], and in the present setup would require further studies by means of a local measurement technique.

In conclusion, the multi-tip coronas give interesting results in stall delay applications, and perform generally much better than the standard wire-to-plate actuator, albeit at the price of a larger power consumption. There is also a performance parameter (mean lift effectiveness) that takes on good values for the wire-to-plate, but at the serious price of a poor discharge stability. In fact, the discharge in a wire-to-plate corona has a dangerous tendency to create arcs, whereas the multi-tip actuators, particularly for high values of r, are more stable, much easier to operate and less sensitive to the external conditions, even if they do not reach the robustness of the DBDs from this point of view. The results reported in this work may help in designing new corona actuators, particularly for applications where humidity and contaminants of the flow can be controlled, i.e. for indoor systems and internal flows. Several applications may arise depending on the flow scale, from the head loss reduction of vanes in small ducts to the stall control inside large ducts, along internal bodies or at the walls in regions of variable section, as may happen in wind tunnel improvements.

References

[1] E. Moreau, Airflow control by non-thermal plasma actuators, J. of Phys. D: Appl. Phys. 40(3) (2007) 605–636.

[2] M. Robinson, Movement of air in the electric wind of the corona discharge, Trans. of the American Inst. of Electr. Engineers, Part I: Communication and Electronics 80(2) (1961) 143–150.

[3] J. Ketcham, H. R. Velkoff, Effect of an electrostatic field on boundary-layer transition, AIAA J. 6(7) (1968) 1381–1383.

[4] S. El-Khabiry, G.M. Colver, Drag reduction by DC corona discharge along an electrically conductive flat plate for small Reynolds number flow, Phys. Fluids 9(3) (1997) 587–599.

[5] G.M. Colver, S. El-Khabiry, Modeling of DC corona discharge along an electrically conductive flat plate with gas flow, IEEE Trans. Ind. Appl. 35(2) (1999) 387–394.

[6] N.E. Jewell-Larsen, S.V. Karpov, I.A. Krichtafovitch, V. Jayanty, C.P. Hsu, A.V. Mamishev, Modeling of corona-induced electrohydrodynamic flow with COMSOL multiphysics, in: Proc. ESA Annual Meeting on Electrostatics, Paper E (Vol. 1), June 2008.

[7] J.C. Mateo-Velez, P. Degond, F. Rogier, A. Seraudie, F. Thivet, Modelling wire-to-wire corona discharge action on aerodynamics and comparison with experiment, J. Phys. D: Appl. Phys. 41(3) (2008) 035205.

[8] G. Artana, J. D'Adamo, L. Leger, E. Moreau, G. Touchard, Flow control with electrohydrodynamic actuators, AIAA J. 40(9) (2002) 1773–1779.

[9] C. Louste, E. Moreau, G. Touchard, Influence of an insulating flat plate on a dc surface corona discharge at various air relative humidities, in: Conference Series-Institute of Physics (Vol. 178), Philadelphia, Institute of Physics, Jan. 2004, 273–278.

[10] A. Labergue, E. Moreau, G. Touchard, A parametric study of surface corona discharge along an insulating flat plate in atmospheric pressure, in: 2005 Annual Report Conference on Electrical Insulation and Dielectric Phenomena, CEIDP'05, Oct. 2005, 490–494.

[11] E. Moreau, L. Leger, G. Touchard, Effect of a DC surface-corona discharge on a flat plate boundary layer for air flow velocity up to 25m/s, J. Electrost. 64(3) (2006) 215–225.

[12] L. Leger, E. Moreau, G. Artana, G. Touchard, Influence of a DC corona discharge on the airflow along an inclined flat plate, J. Electrost. 51 (2001) 300–306.

[13] P. Magnier, D. Hong, A. Leroy-Chesneau, J.M. Pouvesle, J. Hureau, A DC corona discharge on a flat plate to induce air movement, J. Electrost. 65(10) (2007) 655–659.

[14] G. Artana, R. Sosa, E. Moreau, G. Touchard, Control of the near-wake flow around a circular cylinder with electrohydrodynamic actuators, Exp. Fluids 35(6) (2003) 580–588.

[15] A. Labergue, L. Leger, E. Moreau, G. Touchard, J.P. Bonnet, Experimental study of the detachment and the reattachment of an airflow along an inclined wall controlled by a surface corona discharge-application to a plane turbulent mixing layer, IEEE Trans. Ind. Appl. 40(5) (2004) 1205–1214.

[16] A. Labergue, E. Moreau, N. Zouzou, G. Touchard, Separation control using plasma actuators: application to a free turbulent jet, J. Phys. D: Appl. Phys. 40(3) (2007) 674–684.

[17] R. Sosa, G. Artana, E. Moreau, G. Touchard, Stall control at high angle of attack with plasma sheet actuators, Exp. Fluids 42(1) (2007) 143–167.

[18] R. Mestiri, M.M. Oueslati, A.W. Dahmouni, R. Hadaji, S. Ben Nasrallah, F. Aloui, Dynamic Behavior of Printed-Circuits Plasma Actuator Based on DC Electrical Discharge: Application in Aerodynamics, IEEE Trans. Plasma Science 42(7) (2014) 1854–1860.

[19] C. F. Gallo, Corona-a brief status report, IEEE Trans. Industry Appl. (6) (1977) 550–557.

[20] J. R. Roth, Industrial Plasma Engineering: Volume 2-Applications to Nonthermal Plasma Processing (Vol. 2), (2001) CRC press.

[21] M. Samimy, I. Adamovich, J. H. Kim, B. Webb, S. Keshav, Y. Utkin, Active control of high speed jets using localized arc filament plasma actuators, in: AIAA Flow Control Conference, Portland, Oregon, 2004, 2130.

[22] Y. G. Utkin, S. Keshav, J. H. Kim, J. Kastner, I. V. Adamovich, M. Samimy, Development and use of localized arc filament plasma actuators for high-speed flow control, J. of Phys. D: Appl. Phys. 40(3) (2007) 685–694.

[23] E. Moreau, G. Touchard, Enhancing the mechanical efficiency of electric wind in corona discharges, J. Electrost. 66(1) (2008) 39–44.

[24] P. Zhao, S. Portugal, S. Roy, Efficient needle plasma actuators for flow control and surface cooling, Appl. Phys. Lett. 107(3) (2015) 033501.

[25] T.C. Corke, C.L. Enloe, S.P. Wilkinson, Dielectric barrier discharge plasma actuators for flow control, Annual Rev. Fluid Mech. 42 (2010) 505–529.

[26] N. Benard, E. Moreau, Electrical and mechanical characteristics of surface AC dielectric barrier discharge plasma actuators applied to airflow control, Exp. Fluids 55(11) (2014) 1–43.

[27] M. Belan, F. Messanelli, Compared ionic wind measurements on multi-tip corona and DBD plasma actuators, J. Electrost. 76 (2015) 278–287.

[28] F. O. Thomas, T. C. Corke, M. Iqbal, A. Kozlov, D. Schatzman, Optimization of dielectric barrier discharge plasma actuators for active aerodynamic flow control, AIAA J. 47(9) (2009) 2169–2178.

[29] C. C. Wang, R. Durscher, S. Roy, Three-dimensional effects of curved plasma actuators in quiescent air, J. Appl. Phys. 109(8) (2011) 083305.

[30] R. Joussot, A. Leroy, R. Weber, H. Rabat, S. Loyer, D. Hong, Plasma morphology and induced airflow characterization of a DBD actuator with serrated electrode, J. Phys. D: Appl. Phys. 46(12) (2013) 125204.

[31] C. Kim, D. Park, K.C. Noh, J. Hwang, Velocity and energy conversion efficiency characteristics of ionic wind generator in a multistage configuration, J. Electrost. 68(1) (2010) 36–41.

[32] F. Messanelli, M. Belan, Ionic wind measurements on multi-tip plasma actuators, in: European Physical Journal Web of Conferences 114, March 2016, 02073.

[33] J.B. Barlow, W.H. Rae, A. Pope, Low-speed wind tunnel testing, John Wiley and Sons, 1999.

[34] H.C. Garner, E.W. Rogers, W.E. Acum, E.C. Maskell, Subsonic wind tunnel wall corrections, AGARD-OGRAPH 109, Advisory group for aerospace research and development (AGARD), Neuilly-Sur-Seine (France) (1966).

[35] J. Jolibois, M. Forte, E. Moreau, Application of an AC barrier discharge actuator to control airflow separation above a NACA 0015 airfoil: optimization of the actuation location along the chord, J. Electrost. 66(9) (2008) 496–503.

[36] M. Drela, M.B. Giles, Viscous-Inviscid Analysis of Transonic and Low Reynolds Number Airfoils, AIAA J. 25(10) (1987) 1347–1355.

[37] N. Benard, J. Jolibois, E. Moreau, Lift and drag performances of an axisymmetric airfoil controlled by plasma actuator, J. Electrost. 67(2) (2009) 133–139.

[38] L.P. Melton, J. Hannon, C.S. Yao, J. Harris, Active flow control at low Reynolds numbers on a NACA 0015 airfoil, in: 26th AIAA Applied Aerodynamics Conference, August 2008, AIAA 2008-6407, 1–18.

[39] C. He, T.C. Corke, M.P. Patel, Plasma flaps and slats: an application of weakly ionized plasma actuators, J. Aircraft 46(3) (2009) 864–873.

[40] J. Kriegseis, A. Duchmann, C. Tropea, S. Grundmann, On the classification of dielectric barrier discharge plasma actuators: A comprehensive performance evaluation study, J. Appl. Phys. 114(5) (2013) 053301.

[41] S. Bhattacharya, J.W. Gregory, Investigation of the cylinder wake under spanwise periodic forcing with a segmented plasma actuator, Phys. Fluids 27 (2015) 014102.

[42] M. Sato, T. Nonomura, K. Okada, K. Asada, H. Aono, A. Yakeno, Y.Abe, K. Fujii, Mechanisms for laminar separated-flow control using dielectric-barrier-discharge plasma actuator at low Reynolds number, Phys. Fluids 27 (2015) 117101.